Master's Thesis

A simulation study on measurement of the polarization asymmetry A_{LR} using the initial state radiation at the ILC with center-of-mass energy of 250 GeV

(ILCの重心系エネルギー250 GeVにおける初期状態放射を用いたビーム偏極非対称性A_{LR}の測定に関するシミュレーション研究)

Takayuki Ueno

Department of Physics

Graduate School of Science

Tohoku University

2018

Abstract

The future e^+e^- linear collider ILC is expected to be the key of model-independent determination of the couplings of the Higgs boson. In order to achieve this goal, the Higgs Effective Field Theory indicates that the left-right asymmetry A_{LR} needs to be measured more precisely. This study reports the result of a simulation study on measurement of the A_{LR} using the initial state radiation at the ILC with center-of-mass energy of 250 GeV. It is based on a fast SiD simulation in expected ILC condition. The SiD is one of the proposed detectors for the ILC and it is assumed to share the same interaction point with the International Large Detector (ILD) by push-pull configuration.

The event reconstruction is conducted with the method with which the ALEPH experiment in the LEP have measured the beam energy precisely. With the performance of the ILC and the SiD, it is shown that the relativistic statistical error of the A_{LR} is possible to be reduced to about 0.1% assuming the full-running at 250 GeV.

This analysis also implies the utility of the ILC as the Z boson factory.

Contents

Contents **ii**

List of Figures **iv**

List of Tables **vi**

1 Introduction **1**

1.1 Motivtion 1

1.2 Standard Model 2

1.3 Electroweak Interaction 3

1.4 Left-Right Asymmetry 6

2 ILC (International Linear Collider) **8**

2.1 Overview 8

2.2 Accelerator 9

2.2.1 Electron Source 9

2.2.2 Positron Source 10

2.2.3 Damping Ring 11

2.2.4 Main Linac 11

3 SiD (Silicon Detector) **13**

3.1 Overview 13
3.2 PFA (Particle Flow Algorithm) 14
3.3 Silicon-based Tracker 16
3.3.1 Vertex Detector (VTD) 16
3.3.2 Main Tracker 17
3.4 Main Calorimeters 17
3.5 Forward Calorimeter 18
3.6 Solenoidal Magnet and Muon System 18

4 Data Analysis **20**
4.1 Event Generation 20
4.1.1 Conditions of Event Generation 20
4.1.2 ISR VS Process Photon 21
4.2 Data samples 21
4.3 Detector Simulation 23
4.3.1 X Value Reconstruction 23
4.3.2 Quark selection 28
4.4 Results 31
4.4.1 Derivation of the A_{LR} 32
4.4.2 Fitting 35

5 Summary and Future Prospects **41**
5.1 Summary 41
5.2 Future Task 41

Acknowledgement **43**

Reference **44**

List of Figures

2.1 Schematic view of the ILC 9

2.2 Overall Layout of the Electron Source 10

2.3 Overall Layout of the Positron Source 11

2.4 Layout of the Damping Ring 12

2.5 Superconducting niobium nine cell cavity 12

3.1 Layout of the detector hall 15

3.2 Schematic Overview of the SiD 16

3.3 Side View of the Vertex Detector 17

3.4 Layouts of the HCAL barrel (left) and the HCAL endcap (right) 18

3.5 Illustration of the SiD Forward Region 19

4.1 The Feynman diagrams of single-Z production 22

4.2 The Feynman diagrams of single-W production 22

4.3 The Feynman diagram of $e^+e- \to f\bar{f}$ via Z boson production with ISR photon 23

4.4 The Feynman diagrams for the t-channel photon exchange 23

4.5 $M_{f\bar{f}}(true)$ distribution for the $q\bar{q}, \mu^+\mu^-, \tau^+\tau^-$ final states with $(P_{e^-}, P_{e^+}) = (-0.8, +0.3)$. 24

4.6 $M_{f\bar{f}}(true)$ distribution for the $q\bar{q}, \mu^+\mu^-, \tau^+\tau^-$ final states with $(P_{e^-}, P_{e^+}) = (+0.8, -0.3)$ 25

4.7 Illustration of the COM frame of e^+e^- 25
4.8 Illustration of the COM frame of e^+e^- after ISR 27
4.9 The number of charged tracks distribution 29
4.10 The dependence of the significance on number of charged tracks 30
4.11 The lowest-order Feynman diagrams for semi-leptonic decay of W^+W^- . . . 30
4.12 ρ distribution 31
4.13 The dependence of the significance on ρ 32
4.14 The M_{reco} distribution 33
4.15 The dependence of the significance on M_{reco} 34
4.16 The x distribution before the selection cut with $(P_{e^-}, P_{e^+}) = (-0.8, +0.3)$ . . 35
4.17 The x distribution after the selection cut with $(P_{e^-}, P_{e^+}) = (-0.8, +0.3)$ . . . 36
4.18 The dependence of the significance on x 37
4.19 The x distribution of background events with $(P_{e^-}, P_{e^+}) = (-0.8, +0.3)$ . . . 37
4.20 The x distribution of background events with $(P_{e^-}, P_{e^+}) = (+0.8, -0.3)$ . . . 38
4.21 Fitting for the x distribution of signal events with $(P_{e^-}, P_{e^+}) = (-0.8, +0.3)$ 38
4.22 Fitting for the x distribution of signal events with $(P_{e^-}, P_{e^+}) = (+0.8, -0.3)$ 39
4.23 Fitting for the x distribution of total events with $(P_{e^-}, P_{e^+}) = (-0.8, +0.3)$. 39
4.24 Fitting for the x distribution of total events with $(P_{e^-}, P_{e^+}) = (+0.8, -0.3)$. 40

List of Tables

1.1 Table for the relation among Q, T_3 and Y 4

3.1 Key parameters of the baseline SiD design (based on the TDR) 14

4.1 Simulation conditions 21

4.2 cross section for various processes in this study 26

4.3 Number of all events and background events 32

4.4 The result of integration for each fitting function in the range of $0.75 < x < 0.95$ 36

Chapter 1

Introduction

1.1 Motivtion

The Standard Model (SM) is the theory describing the electromagnetic, weak, and strong interactions and classifying all elementary particles. With this theory, we have unlocked many mysteries in elementary particle physics. The discovery of Higgs boson in July 2012 by the Large Hadron Collider (LHC) means the last puzzle piece of the SM has been placed [1]. Even though its properties were found to be similar to those of the Higgs boson predicted by the SM, many theories which imply physics beyond the SM have been proposed and their predictions need experimental validation.

The LHC is a proton-proton collider, where the colliding particles are relatively heavy and therefore the center-of-mass energy (COM) is high. Because of that, it is suitable for searching a new particle. However, the proton is a composite particle, consisting of three quarks and gluons, and therefore initial constituents and energies differ each time. In addition, both strong force and electromagnetic force work when protons are made to collide. That is why the number of background events is extremely high. On the other hand, the ILC is an electron-positron collider, where the colliding particles are point-like and the background is

much less compared to the LHC. Due to this feature, it will be possible to measure the Higgs boson properties more precisely.

The ILC will start operating with a COM of 250 GeV and it will be increased step by step. In the $\sqrt{s}$ =250 GeV operation, the Effective Field Theory (EFT) is significant in that, its coupling constants, showing the deviation from the SM, can be measured model independently. In the frame of this theory, five terms are involved in the deviation of the effective weak mixing angle from the SM. If the incoming beams can be polarized, the variable that is the most sensitive to the effective weak angle is the left-right asymmetry A_{LR} in Z decay. With the precise measurement of the A_{LR} value, one can improve the constraints on these coefficients.

In this study, the procedure to reduce the relativistic statistical error of A_{LR} is investigated by means of a simulation of Z production from two beams followed by a decay to a fermion-pair.

1.2 Standard Model

The Standard Model (SM) is the most successful theory in particle physics and describes a wide range of properties of elementary particles [2]. All known elementary particles are classified into quarks, leptons, gauge bosons and scalar bosons. There are six quarks (up, down, charm, strange, top, and bottom) and six leptons (electron, electron neutrino, muon, muon neutrino, tau and tau neutrino) and all of these particles are collectively called fermion. Gauge bosons are particles that mediate fundamental forces. Photons mediate the electromagnetic interaction, $W^{\pm}$, Z bosons the weak interaction and gluons the strong interaction respectively. The only particle scalar bosons include is Higgs boson, which is responsible for the masses of quarks, leptons and vector bosons.

1.3 Electroweak Interaction

The electroweak interaction is the unified description of electroweak and weak interaction under a $SU(2)_L \otimes U(1)_Y$ gauge group in the SM [3]. This is based on the GWS theory, the work of three physicists Sheldon Lee Glashow, Steven Weinberg and Abdus Salam [4][5][6]. Due to spontaneous symmetry breaking from SU(2) $\otimes$ U(1) into the pure QED part, $U(1)_{em}$ and the interactions of the heavy gauge bosons, Z and W. The interaction can be distinguished into the charged current interaction, mediated by the W^+ or W^- boson and the neutral current interaction, mediated by the Z boson. The gauge bosons and coupling constant corresponding to SU(2) are W_i^μ (i = 1,2,3) and g, as for U(1), the B boson and g'. Then, the photon and Z^0 boson are related with W_3^μ and the B boson by

$$\begin{pmatrix} A^\mu \\ Z^\mu \end{pmatrix} = \begin{pmatrix} \cos\theta_{\mathrm{w}} & \sin\theta_{\mathrm{w}} \\ -\sin\theta_{\mathrm{w}} & \cos\theta_{\mathrm{w}} \end{pmatrix} \begin{pmatrix} B^\mu \\ W_3^\mu \end{pmatrix}, \tag{1.1}$$

where θ_{w} is the weak mixing angle. A_μ and Z_μ correspond to photon and Z^0 boson respectively.

Invariance of Dirac equation under SU(2) and U(1) transformations requires replacing the gradient ∂^μ by the covariant derivative D^μ [7]:

$$\partial^\mu \rightarrow D^\mu = \partial^\mu - igT_iW_i^\mu - ig'\frac{Y}{2}B^\mu, \tag{1.2}$$

where T_i (i = 1, 2, 3) stands for a generator of SU(2) group, and Y, the weak hypercharge. Only the terms concerning W_3^μ and B^μ is given by

$$gW_3^\mu T_3 + g'B^\mu\frac{Y}{2} = [g\cos\theta_{\mathrm{W}}T_3 - g'\sin\theta_{\mathrm{W}}\frac{Y}{2}]Z^\mu + [g\sin\theta_{\mathrm{W}}T_3 + g'\cos\theta_{\mathrm{W}}\frac{Y}{2}]A^\mu \tag{1.3}$$

The matrix combining A^μ must be eQ:

$$g \sin\theta_{\rm W} T_3 + g' \cos\theta_{\rm W} \frac{Y}{2} = eQ = e(T_3 + \frac{Y}{2}), \tag{1.4}$$

where Q stands for the electric charge and e is the coupling constant for the electromagnetic interaction. Here, the Gellmann-Nishijima relation is introduced:

$$Q = T_3 + \frac{Y}{2} \tag{1.5}$$

The eigenvalues of Q, T_3 and Y for the all fermions in the SM are summarized in Table 1.1 Then, the weak mixing angle $\theta_{\rm W}$ and the coupling constant for the electromagnetic interaction

	Electric Charge Q	Weak Isospin T_3	Weak Hyper-Charge Y
ν_{eL}, $\nu_{\mu L}$, $\nu_{\tau L}$	0	+1/2	−1
e^-_L, μ^-_L, τ^-_L	−1	−1/2	−1
e^-_R, μ^-_R, τ^-_R	−1	0	−2
u_L, c_L, t_L	+2/3	+1/2	+1/3
d_L, s_L, b_L	−1/3	−1/2	+1/3
u_R, c_R, t_R	+2/3	0	+4/3
d_R, s_R, b_R	−1/3	0	−2/3

Table 1.1: Table for the relation among Q, T_3 and Y

e can be expressed in terms of g and g'

$$\cos\theta_{\rm w} = \frac{g}{\sqrt{g^2 + g'^2}} \tag{1.6}$$

$$\sin\theta_{\rm w} = \frac{g'}{\sqrt{g^2 + g'^2}} \tag{1.7}$$

$$e = g \sin\theta_{\rm w} = g' \cos\theta_{\rm w} = \frac{gg'}{\sqrt{g^2 + g'^2}} \tag{1.8}$$

On the other hands, the matrix combining with Z^μ can be translated as

$$g \cos\theta_{\rm W} T_3 - g' \sin\theta_{\rm W} \frac{Y}{2} = \frac{g}{\cos\theta_{\rm W}} (T_3 - \sin^2\theta_W Q) \tag{1.9}$$

Therefore, the lagrangian for Z-fermion interactions can be expressed as

$$\mathcal{L} = \frac{g}{\cos\theta_{\rm W}} Z_\mu \bar{\Psi} \gamma^\mu (s_L P_L + s_R P_R) \Psi, \tag{1.10}$$

where $P_{L,R}$ is a projection operator and defined as

$$P_L \equiv \frac{1 - \gamma_5}{2} \qquad P_R \equiv \frac{1 + \gamma_5}{2} \tag{1.11}$$

The right-handed and left-handed components are defined by

$$\Psi_L \equiv P_L \Psi \qquad \Psi_R \equiv P_R \Psi \tag{1.12}$$

In addition, $s_{L,R}$ is the eigenvalue of $T_3 - \sin\theta_{\rm W}^2 Q$ for left/right-handed fermion. Particularly, in the case of Z-electron interaction, they are obtained by

$$s_R = \sin^2\theta_{\rm w} \qquad s_L = -\frac{1}{2} + \sin^2\theta_{\rm w}, \tag{1.13}$$

which can be derived from Table 1.1.

$W^\pm$ is expressed by the linear combination of W_μ^1 and W_μ^2.

$$W^\pm = \frac{1}{\sqrt{2}} (W_\mu^1 \mp i W_\mu^2) \tag{1.14}$$

$W^{\pm}$ bosons can couple only left-handed fermion, while Z^0 boson can couple both left-handed and right-handed fermions because of the weak mixing angle.

1.4 Left-Right Asymmetry

The left-right cross-section asymmetry A_{LR} is defined as

$$A_{LR} \equiv \frac{\sigma_L - \sigma_R}{\sigma_L + \sigma_R}, \tag{1.15}$$

where $\sigma_{L,R}$ describes the cross sections for the Z bosons with 100 % left/right-handed electron bunch. However, in the actual measurement, the magnitude of the beam polarization needs to be taken into account. If the magnitude of luminosity-weighted electron/positron polarization is expressed as $\langle P_{e^-} \rangle$ / $\langle P_{e^+} \rangle$, A_{LR} can be translated as

$$A_{LR} = \frac{\sigma_L^{meas} - \sigma_R^{meas}}{\sigma_L^{meas} + \sigma_R^{meas}} \frac{1 + \langle P_{e^-} \rangle \langle P_{e^+} \rangle}{\langle P_{e^-} \rangle + \langle P_{e^+} \rangle}, \tag{1.16}$$

where $\sigma_{L,R}^{meas}$ indicates the cross sections for the Z bosons with 80 % left/right-handed electron bunch in this study. Based on the ILC baseline, $\langle P_{e^-} \rangle$ is assumed to be 0.8 and $\langle P_{e^+} \rangle$ is 0.3. Assume that the integrated luminosity and the magnitude of the beam polarization are helicity-symmetric. The A_{LR} is given by

$$A_{LR} = \frac{N_L - N_R}{N_L + N_R} \frac{1 + \langle P_{e^-} \rangle \langle P_{e^+} \rangle}{\langle P_{e^-} \rangle + \langle P_{e^+} \rangle} \tag{1.17}$$

According to [8], although the measured A_{LR} have to be corrected due to the effect of ISR and γ-Z interference, the relative correction is estimated at an approximately 2.0 % and can be controlled.

Particularly, this study is focused on A_{LR} at the Z-electron interaction. Due to the square

of the coupling constant being proportional to the cross section, A_{LR} can be related to $\sin^2\theta_{\mathrm{W}}$ as:

$$\begin{aligned} A_{LR} &\equiv \frac{\sigma_L - \sigma_R}{\sigma_L + \sigma_R} \\ &= \frac{s_L^2 - s_R^2}{s_L^2 + s_R^2} \\ &= \frac{(-\frac{1}{2} + \sin\theta_{\mathrm{w}})^2 - (\sin\theta_{\mathrm{w}})^2}{(-\frac{1}{2} + \sin\theta_{\mathrm{w}})^2 + (\sin\theta_{\mathrm{w}})^2} \\ &= \frac{2(1 - 4\sin^2\theta_{\mathrm{w}})}{1 + (1 - 4\sin^2\theta_{\mathrm{w}})^2}, \end{aligned} \tag{1.18}$$

where the result of Equation(1.12) is used.

Currently, the most precise measurement of A_{LR} comes from the data taken in SLD detector at SLAC National Accelerator Laboratory[8]. The present value has the relative error of approximately 1.5 % The goal of this study is to estimate how this error can be reduced at the ILC with center-of-mass energy of 250 GeV.

Chapter 2

ILC (International Linear Collider)

2.1 Overview

The International Linear Collider (ILC) is a future electron-positron collider with a center-of-mass (COM) energy of 250 GeV. One of the merits a linear collider has is extensibility and therefore higher COM energy operation is technically possible expected depending on the result at 250 GeV. In 2013, a technical design report (TDR) [9] was published which treats the details of expected physics, accelerator and detectors. The following part is described based on this report.

The pillars of the ILC physics program are the precise measurement of the properties of the Higgs boson, the precise measurement of the top quark and the validation of physics beyond the Standard Model (BSM). Three key features of the ILC make these studies possible. First, it is easy to arrange the COM energy so that it can measure a threshold corresponding to each physical motivation. Second, the initial state is well known due to it being a lepton-lepton collider. Finally, electron/positron beams can be polarized up to 80%/30%. This availability is a big advantage in the validation of the electroweak theory, because left-handed and right-handed fermions are treated separately in electroweak interactions.

This section presents physics at the ILC and the accelerator system.

2.2 Accelerator

The ILC accelerator primarily consists of Electron/Positron Source, Damping Ring and Main Linac. The two beams generated by the Electron/Positron Source are focused in the Damping Ring and then accelerated in the Main Linac and then made to collide with each other. The layout of the ILC is shown in Figure 2.1. Following is a brief description of each system.

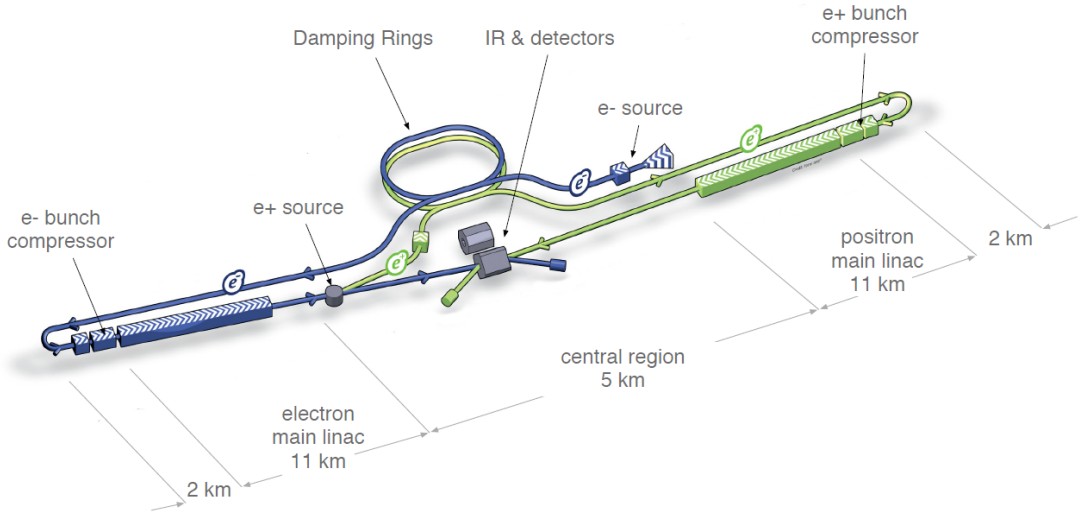

Figure 2.1: Schematic view of the ILC

2.2.1 Electron Source

The layout of the electron source is shown in Figure 2.2. A polarized laser illuminates a strained GaAs photocathode, so that polarized electrons are emitted due to the photoelectric effect. This system aims for a polarization of 80%. Bunches consisting of emitted electrons are accelerated to 76 MeV in normal-conducting structures and then accelerated to 5 GeV in a superconducting linac. Their spins are rotated in the vertical direction compared to their

traveling direction by the Linac-to-Ring transfer line before injection into the damping ring.

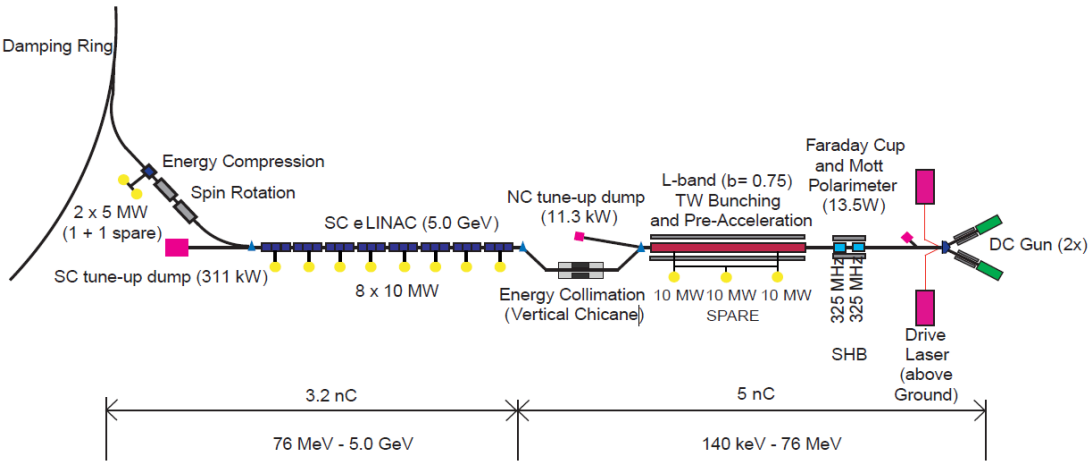

Figure 2.2: Overall Layout of the Electron Source

2.2.2 Positron Source

The layout of the positron source is shown in Figure 2.3. Polarized positrons are generated by the primary electron beam after acceleration in the main linac. The beam is taken to a 147 m superconducting helical undulator and provides photons with energies of 10-30 MeV due to synchrotron radiation. The photons collide with a Ti-alloy target, so that a beam of electron positron pairs is produced. After acceleration to 125 MeV, beam and remaining photons are separated from positrons by a magnetic field and dumped, giving a positron beam. The positron beam is accelerated to 400 MeV in normal-conducting structures and then accelerated to 5 GeV in a superconducting linac. The spin is rotated into the vertical in the same way as the electron beam. After that, the beam is injected to the damping ring by the kicker magnet. The baseline design provides a polarization of 30%.

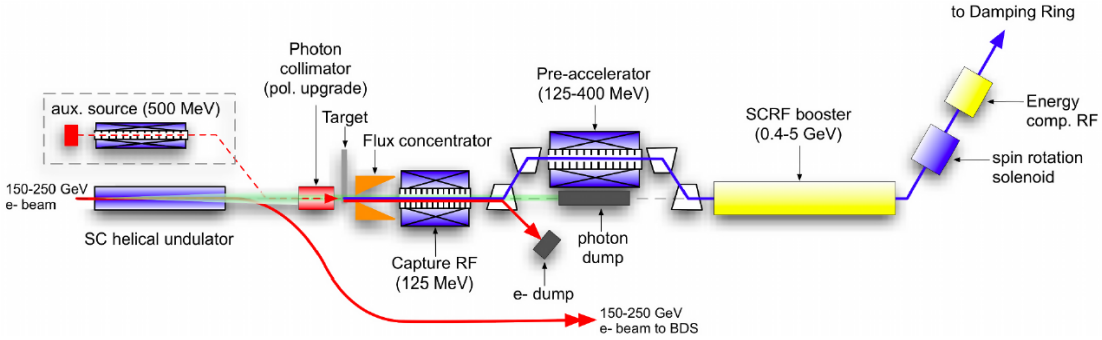

Figure 2.3: Overall Layout of the Positron Source

2.2.3 Damping Ring

The layout of the damping ring is shown in Figure 2.4. The damping rings consisting of one electron ring and one positron ring are operated at a beam energy of 5 GeV, each with a circumference of 3.2 km. They include circular sections and straight sections. Each beam loses energy in the circular sections due to synchrotron radiation, while the direction of the beam is not changed, because emitted photons travel colinearly. After that, each beam is accelerated in the direction of the beam traveling in the straight sections. This system results in the decrease of the beam emittance, giving higher luminosity at the collision point.

2.2.4 Main Linac

The beam is accelerated to 15 GeV, while it is transported from a damping ring to the Main Linacs. The beam is accelerated in approximately 7,400 superconducting nine-cell cavities (see Figure 2.5) The average accelerating gradient of each cavity is 31.5 MV/m.

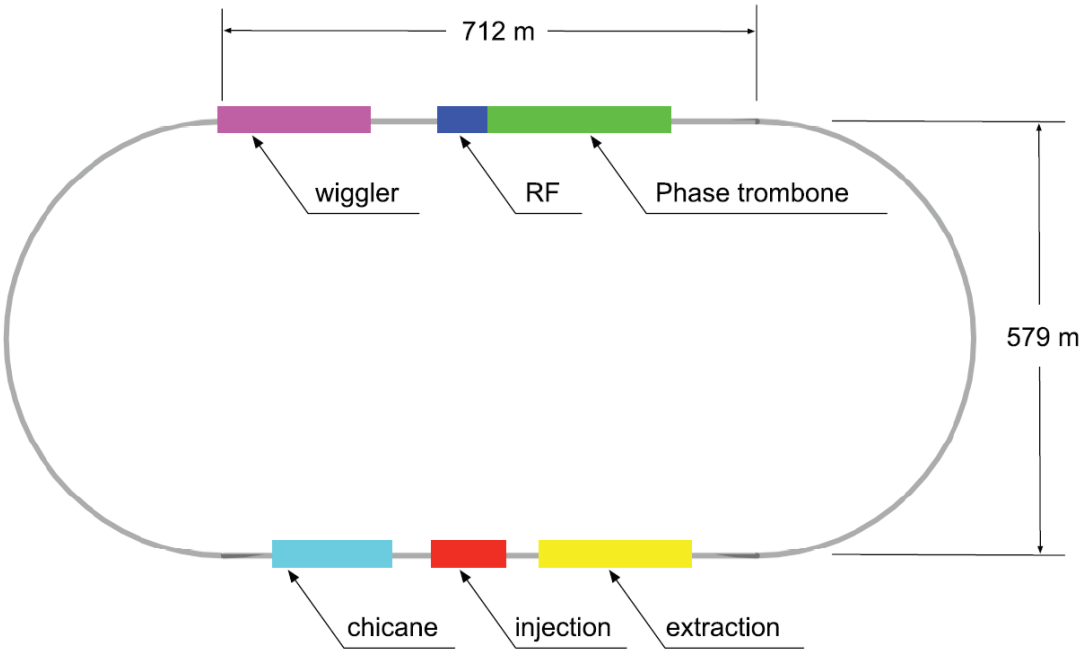

Figure 2.4: Layout of the Damping Ring

Figure 2.5: Superconducting niobium nine cell cavity

Chapter 3

SiD (Silicon Detector)

3.1 Overview

The ILC has two candidate detectors, the International Large Detector (ILD) and the Silicon Detector (SiD), which share the same detector hall using a push-pull system. The arrangement of the two detectors in the central region is shown in Figure 3.1. Both detector designs are optimized for Particle Flow Algorithm (PFA) and flavor tagging. The PFA is a method for achieving high jet energy resolution, and flavor tagging is needed for the identification of the flavor of the quark giving rise to a high-energy jet. The following are the components of the SiD.

- Silicon-based Tracking
  - Vertex Detector (VTD)
  - Main Tracker
- Calorimeter
  - Electromagnetic Calorimeter (ECAL)
  - Hadronic Calorimeter (HCAL)

- Outer layers
  - Return Yoke / Muon System
  - Superconducting Solenoidal Coil

The schematic overview of the SiD is shown in Figure 3.2. The key parameters of the SiD design are summarized in Table 3.1. (All dimension are given in cm).

SiD barrel	Technology	Inner radius	Outer radius	z extent
Vertex Detector	Silicon pixels	1.4	6.0	±6.25
Tracker	Silicon strips	21.7	122.1	±152.2
ECAL	Silicon pixels-W	126.5	140.9	±176.5
HCAL	RPC-steel	141.7	249.3	±301.8
Solenoid	5 Tesla SC	259.1	339.2	±298.3
Flux return	Scintillator-steel	340.2	604.2	±303.3

SiD Endcap	Technology	Inner radius	Outer radius	z extent
Vertex detector	Silicon pixels	7.3	83.4	16.6
Tracker	Silicon strips	77.0	164.3	125.5
ECAL	Silicon pixel-W	165.7	180.0	125.0
HCAL	RPC-steel	180.5	302.8	140.2
Flux return	Scintillator / steel	303.3	567.3	604.2
LumiCal	Silicon-W	155.7	170.0	20.0
BeamCal	Semiconductor-W	277.5	300.7	13.5

Table 3.1: Key parameters of the baseline SiD design (based on the TDR)

3.2 PFA (Particle Flow Algorithm)

Important events expected at the ILC often contain jets, which are bundles of charged hadrons, neutral hadrons and photons resulting from hadronization. The energy resolution of the HCAL is the worst among the components of the SiD. On the other hand, regarding

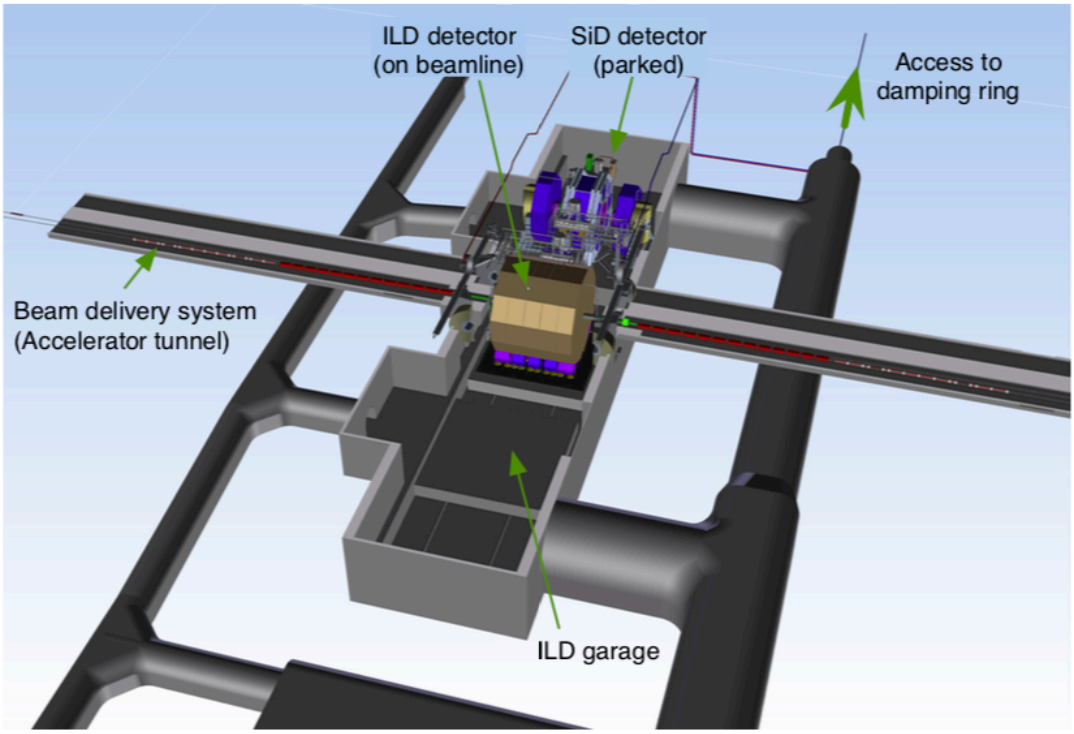

Figure 3.1: Layout of the detector hall

charged hadrons, the silicon tracker performs best. The jet energy resolution can be maximized by measuring charged particles in the silicon tracker, photons in the electromagnetic calorimeter (ECAL) and neutral hadrons in the hadron calorimeter (HCAL). In a typical jet, 60% of the energy is in form of charged hadrons, 30% in form of photons and 10% in form of neutral hadrons. It means that by correctly identifying the hits from each particle, we can use the detectors with the worst resolution for only 10% of the measurement, and the best detectors for 60%. This requires excellent interplay of all components, and the SiD has been designed to satisfy this requirement.

The following shows the procedure to reconstruct jets by the PFA method.

1. reconstruct charged tracks and electrons and muons in the silicon tracker
2. identify and exclude charged hadrons and electrons and muons in the calorimeters

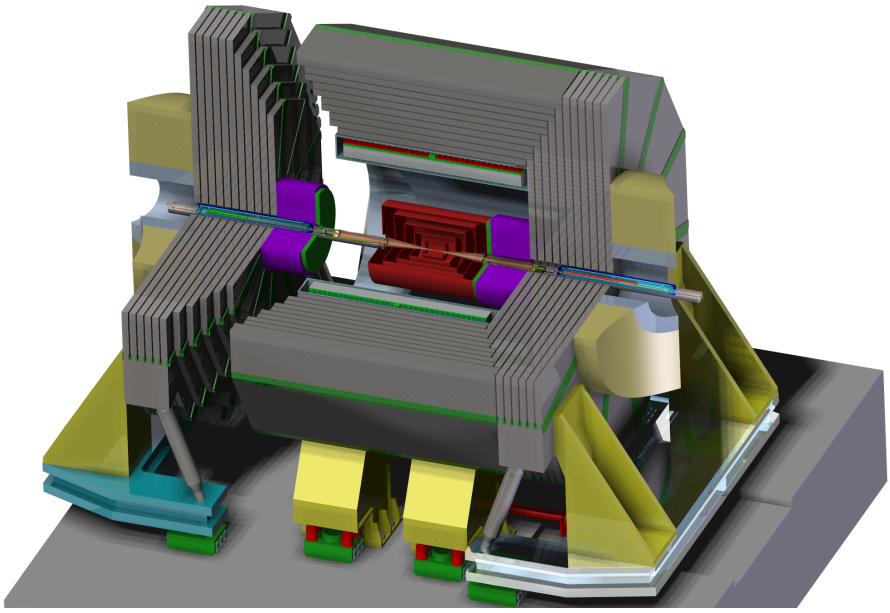

Figure 3.2: Schematic Overview of the SiD

3. reconstruct photons in the ECAL
4. reconstruct neutral hadrons in the HCAL
5. reconstruct jet energy using the above information

3.3 Silicon-based Tracker

The silicon-based Tracker consists of vertex detector and main tracker. The PFA is supported by the use of silicon sensors, giving excellent tracking with superb efficiency and two-particle separation.

3.3.1 Vertex Detector (VTD)

To explore unknown physical mechanism of new observed processes, the identification of heavy flavors will be a key approach. The vertex detector, which is installed at the innermost layers, supports heavy flavor identification. Particularly, in the ILC, it is required to identify,

whether jets originate from either b-quarks or c-quarks with high precision. At the designing stage, three-dimensional point resolution, a very low material budget to minimize multiple Coulomb scattering and the readout speed must be considered. The side view of the vertex detector is shown in Figure 3.3.

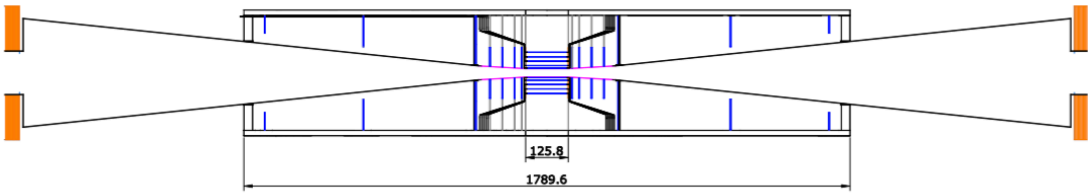

Figure 3.3: Side View of the Vertex Detector

3.3.2 Main Tracker

The main tracker consists of five cylinders in the central region and four disks in each of the end regions. With an outer cylinder radius of 1.25 m and a 5 T solenoidal magnetic field, the high resolution of the charged track momentum is accomplished at the level of $\delta(1/p_T) = 5 \times 10^{-5}/[\text{GeV/c}]$.

3.4 Main Calorimeters

The SiD components are arranged so that the PFA approach works properly. This requires the main calorimeters to associate tracks and energy deposits and follow the track correctly. This led to the design decision to have the calorimeters inside the solenoid magnet. The electromagnetic and hadronic sections consist of a central barrel part and two endcaps. The electromagnetic calorimeter (ECAL) has silicon in the active layers, put between tungsten absorber layers. The total depth of the ECAL corresponds to 26 radiation lengths (X_0). The hadronic calorimeter (HCAL) consists of steel plates and active layers using scintillator tiles

and they are arranged alternately. The total depth of the HCAL is 4.5 nuclear interaction lengths. Figure 3.4 shows the layout of the HCAL barrel and the HCAL endcap.

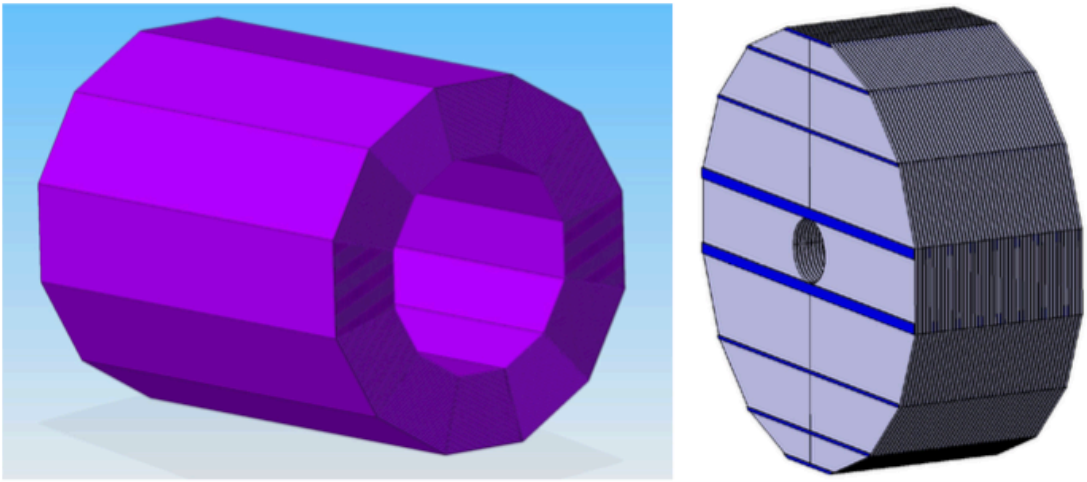

Figure 3.4: Layouts of the HCAL barrel (left) and the HCAL endcap (right)

3.5 Forward Calorimeter

The LumiCal measures the luminosity precisely and the BeamCal provides the fast estimation of the luminosity. The LumiCal is placed in a hole in the endcap of the ECAL and uses silicon pixel readout. The BeamCal is a device for measuring low-energy electron-positron pairs resulted from beamstrahlung so that a bunch-by-bunch luminosity can be given. Figure 3.5 illustrates the SiD forward region.

3.6 Solenoidal Magnet and Muon System

The superconducting solenoidal magnet has a 5 T magnet field, enabling the SiD to be compact. The crucial role of the flux-return yoke is to prevent magnet flux leakage and to

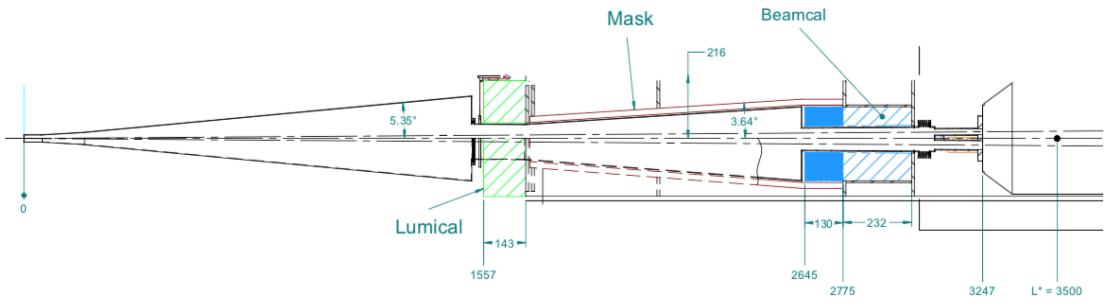

Figure 3.5: Illustration of the SiD Forward Region

serve as a muon detector. Muons arising from beam collision penetrate the calorimeters. Scintillator tiles are installed in the flux return yoke to tag such muons.

Chapter 4

Data Analysis

4.1 Event Generation

4.1.1 Conditions of Event Generation

Data samples analyzed in this study are based on the Detailed Baseline Design (DBD) [9] generated by Whizard 1.95 [10] , which is a universal program system for elementary processes at colliders. Whizard includes the Optimized Matrix Element Generator, O'Mega [11] , for generating tree-level matrix elements for arbitrary elementary processes. Parton shower and hadronization are performed by Pythia 6.4 [12], and tau decays are simulated by TAUOLA [13]. The beam spectrum simulation is conducted by CIRCE2. The polarization of both beams are assumed to be $P(e^-, e^+) = (\mp 80\%, \pm 30\%)$. The samples are generated with ISR options, but process photon is not included in the final state as Whizard input. Table 4.1 summarizes the simulation conditions in this study.

Parameter		Value
COM Energy	$\sqrt{s}$	250 GeV
Integral luminosity	L	250 fb^{-1} for each polarization
Beam Polarlization	(P_{e^-}, P_{e^+})	$(-0.8, +0.3), (+0.8, -0.3)$
Weak Maxing Angle	$\sin\theta_{\mathrm{W}}$	0.22225

Table 4.1: Simulation conditions

4.1.2 ISR VS Process Photon

As mentioned above, there are two choices to get photon stemming from beams in Whizard; turning on ISR option or including photon in the process definition. Here, the former is called ISR photon, and the latter is called process photon. The ISR photon is dealt with approximately, in that it travels completely collinear to the beam axis. Practically, due to helicity conservation, the helicity of electron/positron beam is flipped in the $e \to e\gamma$ splitting process. In spite of that, it is arranged that helicity splitting does not occur in order to simplify the situation. On the other hand, in the case of process photon, its angular distribution is calculated by using a matrix element, where the factor of helicity-flipping is proportional to m_e. In this study, ISR photon is used as a primary step to process photon.

4.2 Data samples

The samples include events of $\gamma\gamma$, γe^+ or $e^-\gamma$ for initial states, which are not overlaid with other events in this study. Hence, they are handled as independent events in spite of secondary events at single e^+e^- collision. The samples also have events of $e^+e^- \to f\bar{f}$ and $e^+e^- \to ZZ, W^+W^-, \text{single-Z}, \text{single-W} \to 4$ fermions. The examples of the Feynman diagrams of single-Z production and single-W production events are depicted in Figure 4.1 and Figure 4.2.

Figure 4.3 shows the Feynman diagram of $e^+e^- \to f\bar{f}$ via Z boson production with ISR

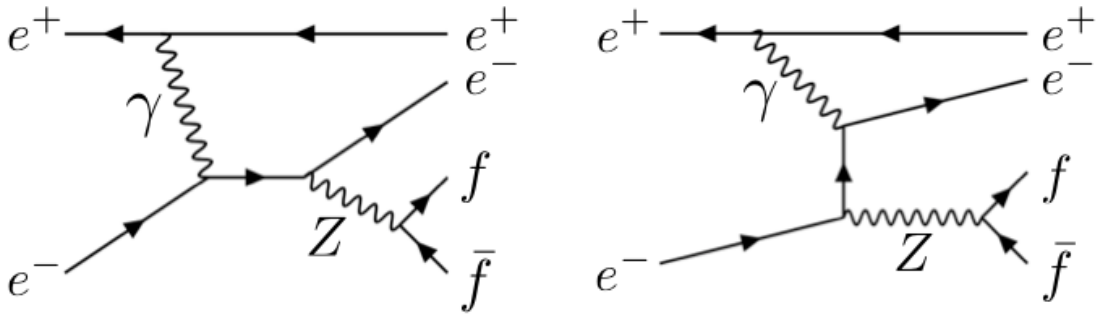

Figure 4.1: The Feynman diagrams of single-Z production

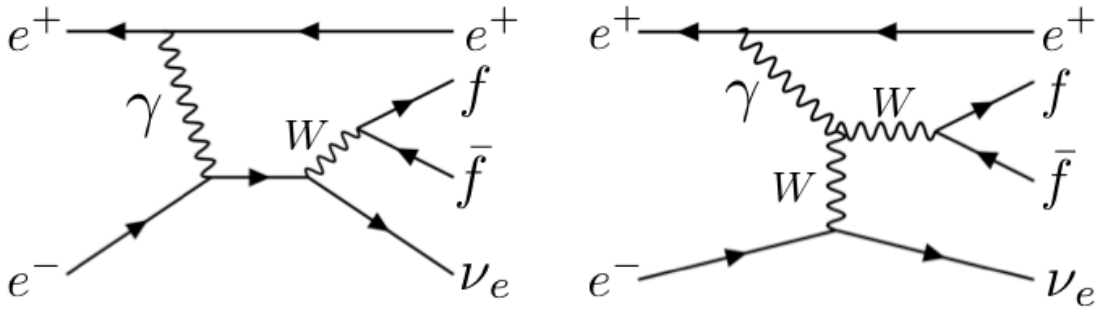

Figure 4.2: The Feynman diagrams of single-W production

photon. The A_{LR} measurement depends only on initial beam state, which are well known for the ILC, and it is irrespective of the final state. However, e^+e^- final states are excluded from signal because the t-channel photon exchange processes dilute the A_{LR} value (see Figure 4.4). Figure 4.5 and 4.6 shows the $M_{f\bar{f}}(true)$ distributions for the $q\bar{q}, \mu^+\mu^-, \tau^+\tau^-$ final states. In the region of the Z resonance, the total cross section is dominated by the Z exchange process and it primarily consists $q\bar{q}$ final state. Therefore, in this study, the signal events are defined as $q\bar{q}$ final state whose invariant mass is between 71 GeV and 111 GeV. It is assumed that q contains all quarks except top quark because top quark is too heavy to be pair-produced in Z decays. Another peak near 250 GeV is primarily caused by γ/Z^* exchange process.

Table 4.2 summarizes the cross sections for various processes in this study.

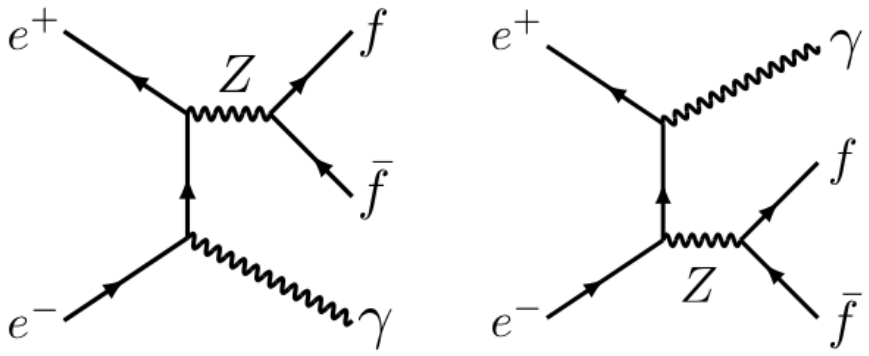

Figure 4.3: The Feynman diagram of $e^+e- \to f\bar{f}$ via Z boson production with ISR photon

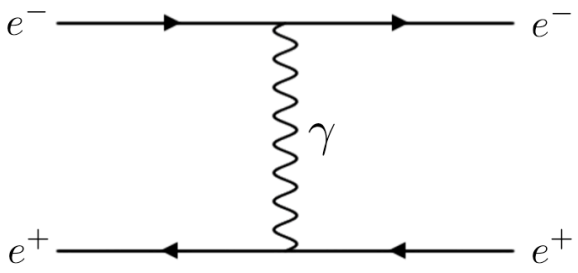

Figure 4.4: The Feynman diagrams for the t-channel photon exchange

4.3 Detector Simulation

The detector simulation is conducted by Delphes 3.4.1, which is a parametric detector simulation. In this study, we use the DSiD parameters [14] . The SiD design and performance are based on the DBD.

4.3.1 X Value Reconstruction

In order to reconstruct the effective COM energy $\sqrt{s'}$, we follow the method used in the ALEPH at LEP to measure the beam energy with high precision. The x is a parameter regarding the effective COM energy and defined as the ratio of the ISR photon energy to the

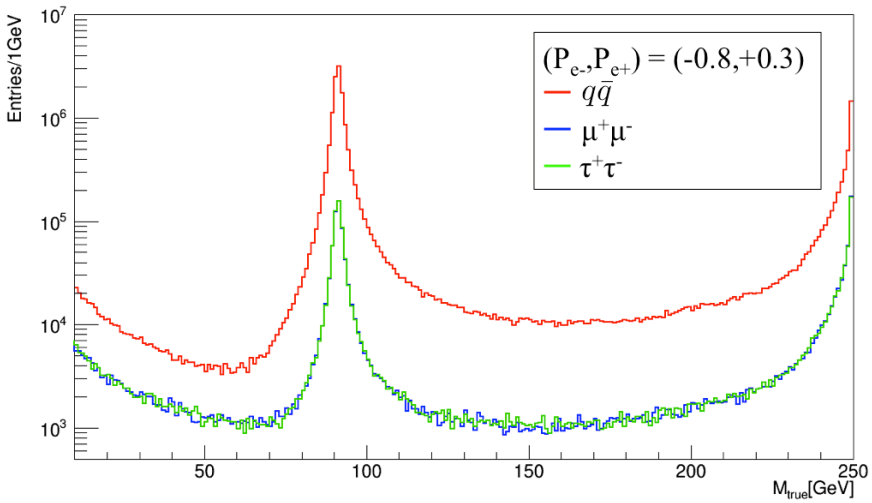

Figure 4.5: $M_{f\bar{f}}(true)$ distribution for the $q\bar{q}, \mu^+\mu^-, \tau^+\tau^-$ final states with $(P_{e^-}, P_{e^+}) = (-0.8, +0.3)$.

beam energy [15].

$$x \equiv \frac{E_\gamma}{E_{beam}} \tag{4.1}$$

Assume that, in the COM frame, the nominal energy of each beam is E and the ISR photon energy is xE. (see Figure 4.7) The nominal COM energy $\sqrt{s}$ is given by

$$\sqrt{s} = \sqrt{4E_1E_2} = \sqrt{4E^2} \tag{4.2}$$

Then, the effective COM energy $\sqrt{s'}$ can be expressed as

$$\sqrt{s'} = \sqrt{4E(E - xE)} = \sqrt{4E^2(1-x)} = \sqrt{s(1-x)}. \tag{4.3}$$

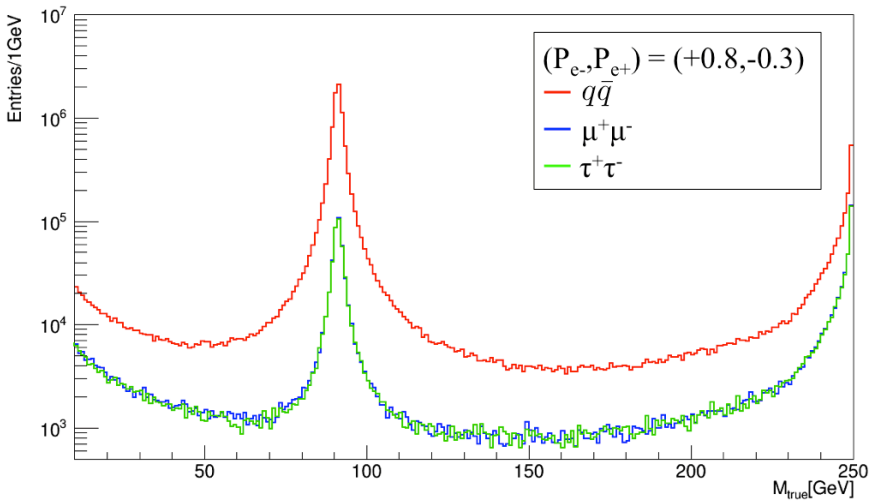

Figure 4.6: $M_{f\bar{f}}(true)$ distribution for the $q\bar{q}, \mu^+\mu^-, \tau^+\tau^-$ final states with $(P_{e^-}, P_{e^+}) = (+0.8, -0.3)$

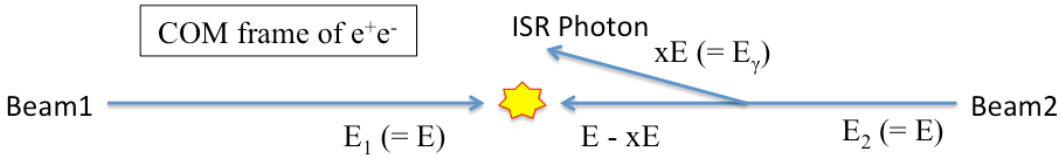

Figure 4.7: Illustration of the COM frame of e^+e^-

ISR photon is assumed to be emitted along the beam pipe and boost the COM frame in that direction with the magnitude of the boost $|\beta|$. Then, β is expressed as

$$|\beta| = \frac{P_{tot}}{E_{tot}} = \frac{xE}{E + (E - xE)} = \frac{xE}{E(2 - x)} = \frac{x}{2 - x} \tag{4.4}$$

Therefore x can be written in terms of $|\beta|$:

$$x = \frac{2|\beta|}{1 + |\beta|} \tag{4.5}$$

	Beam Polarization	
Processes	(-0.8,+0.3)	(+0.8,-0.3)
$q\bar{q}$ (71 GeV $< M_{true} <$ 111 GeV)	51.6 [pb]	34.7 [pb]
$q\bar{q}$ (outside 71 GeV $< M_{true} <$ 111 GeV)	26.4 [pb]	11.5 [pb]
e^+e^-	25.2 [pb]	24.6 [pb]
$\mu^+\mu^-$	2.2 [pb]	1.5 [pb]
$\tau^+\tau^-$	2.3 [pb]	1.5 [pb]
4 ferminos (ZZ, W^+W^-, single-Z, single-W)	39.9 [pb]	5.0 [pb]
$\gamma\gamma, e\gamma \to X$	2735 [pb]	2735 [pb]

Table 4.2: cross section for various processes in this study

Then, let's take a look at the relation between the moving directions of fermions and the magnitude of the boost. In order to simplify the situation, jets originating at the collision are assumed to move on the x-y plane, where the x axis is regarded as the moving direction of the ISR photon. If fermion1 has the energy and the momentum (E_1, P_{1x}, P_{1y}) and fermion2 has (E_2, P_{2x}, P_{2y}) in the COM frame of e^+e^- with no ISR , they can be expressed as

$$E_1 = E \qquad P_{1x} = P\cos\theta \qquad P_{1y} = P\sin\theta \tag{4.6}$$

$$E_2 = E \qquad P_{2x} = -P\cos\theta \qquad P_{2y} = -P\sin\theta \tag{4.7}$$

If the energy and the momentum of each jet are viewed in the COM frame of e^+e^- with ISR (see Figure 4.8) , they are given by

$$E'_1 = \gamma E + \eta P\cos\theta \qquad P'_{1x} = \eta E + \gamma P\cos\theta \qquad P'_{1y} = P\sin\theta \tag{4.8}$$

$$E'_2 = \gamma E - \eta P\cos\theta \qquad P'_{2x} = \eta E - \gamma P\cos\theta \qquad P'_{2y} = -P\sin\theta \tag{4.9}$$

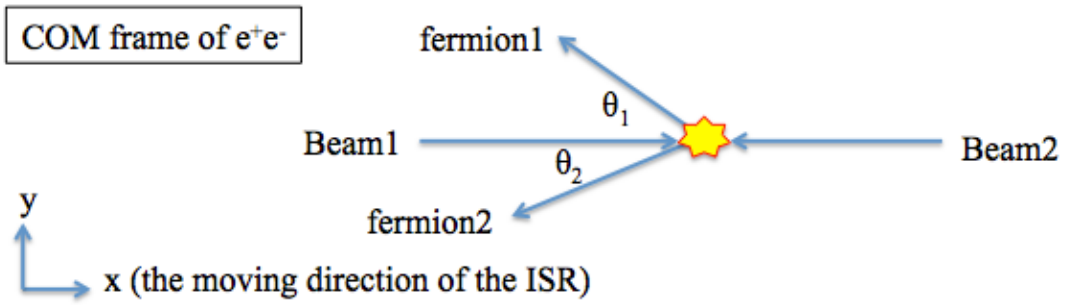

Figure 4.8: Illustration of the COM frame of e^+e^- with ISR

with

$$\gamma \equiv \frac{1}{\sqrt{1-\beta^2}} \qquad \eta \equiv \beta\gamma = \frac{\beta}{\sqrt{1-\beta^2}} \tag{4.10}$$

Define the polar angle of the two jets with respect to direction opposite to the ISR by θ_1, θ_2, then they can be expressed as

$$\begin{aligned} \sin\theta_1 &= \frac{|P'_{1y}|}{E'_1} \qquad & \cos\theta_1 &= \frac{|P'_{1x}|}{E'_1} \\ \sin\theta_2 &= \frac{|P'_{2y}|}{E'_2} \qquad & \cos\theta_2 &= \frac{|P'_{2x}|}{E'_2} \end{aligned} \tag{4.11}$$

Therefore, $|\beta|$ is can be written in terms of θ_1, θ_2:

$$\begin{aligned}
\frac{|\sin(\theta_1+\theta_2)|}{\sin\theta_1+\sin\theta_2} &= \frac{|\sin\theta_1\cos\theta_2+\cos\theta_1\sin\theta_2|}{\sin\theta_1+\sin\theta_2} \\
&= \frac{|P'_{2x}+P'_{1x}|}{E'_2+E'_1} && \text{(using (4.10))} \\
&= \frac{|\eta|}{\gamma} && \text{(using (4.7) and (4.8))} \\
&= |\beta| && \text{(using (4.9))}
\end{aligned} \tag{4.12}$$

Equation (4.4) and (4.11) show that x can be derived from θ_1 and θ_2. The Z boson mass corresponds to the x value of 0.8670.

4.3.2 Quark selection

In order to discriminate between $Z \to q\bar{q}$ (71 GeV $\leq M_{true} <$ 111 GeV) event and other events, the following cuts were applied.

- Number of jets is 2
- 5 ≦ Number of charged tracks ≦ 25
- $\rho < 1.6$
- 50 GeV $< M_{2jet}(reco) <$ 107 GeV

All the cut value above is optimized so that the significance is maximized. The significance S is defined by

$$S \equiv \frac{N_{signal}}{\sqrt{N_{signal}+N_{background}}} \tag{4.13}$$

The jet identification is conducted using anti-k_T algorithm in this study.

The ρ is defined by

$$\rho \equiv \sqrt{2E_l(1-\cos\theta_{l-jet})}, \tag{4.14}$$

where $\cos\theta_{l-jet}$ is the angle for all the combination of charged lepton (e or μ) and a jet. If there is no charged lepton for the final state, the ρ is defined to be zero. As for selected events, all the ρ value needs to be lower than 1.6.

Number of Charged Tracks

This cut plays an important role to reduce events of $\gamma\gamma, e\gamma \to X$. Figure 4.9 shows the number of charged tracks distribution and Figure 4.10 the dependence of the significance on number of charged tracks.

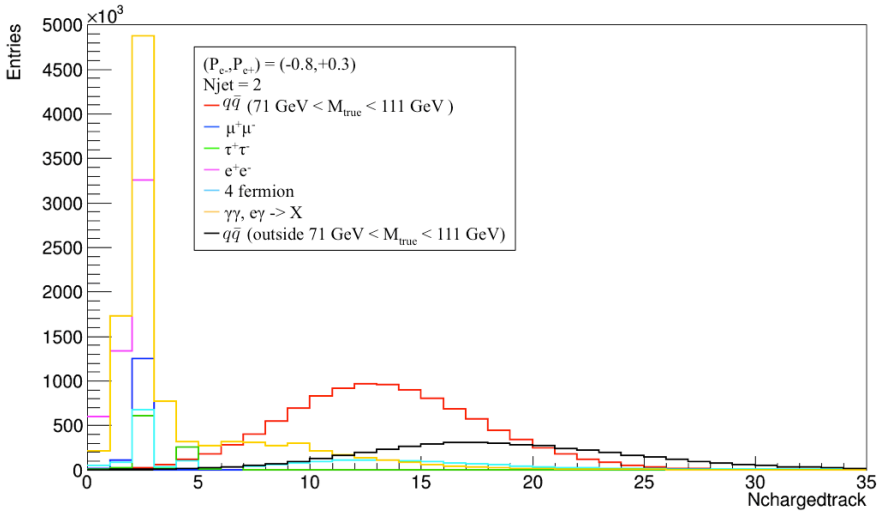

Figure 4.9: The number of charged tracks distribution

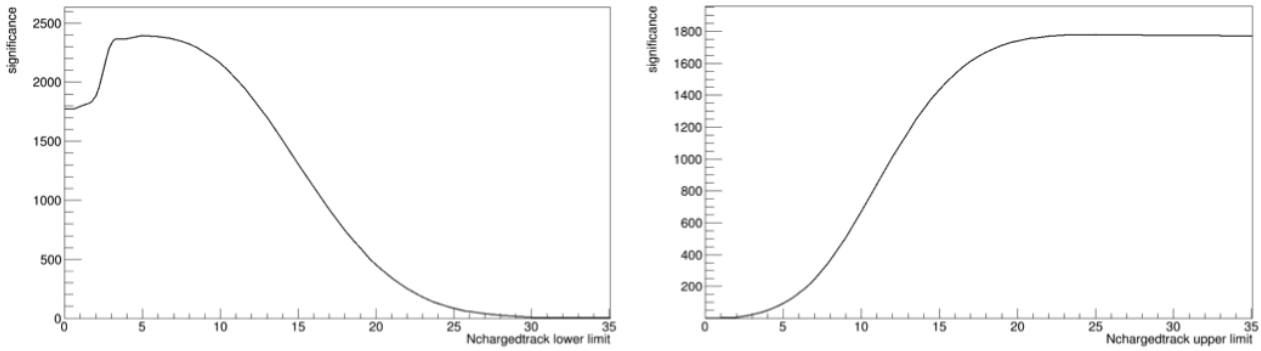

Figure 4.10: The dependence of the significance on number of charged tracks

ρ Value

The ρ value cut is introduced to reduce events of semi-leptonic decays of W^+W^-. (see Figure 4.11 [16]) Two jets originating from semi-leptonic decay of W^+W^- travel in almost the same direction, while a charged lepton is isolated. Therefore, the ρ tends to be relatively high in these cases. The ρ distribution is shown in Figure 4.12 and the dependence of the significance on ρ in Figure 4.13.

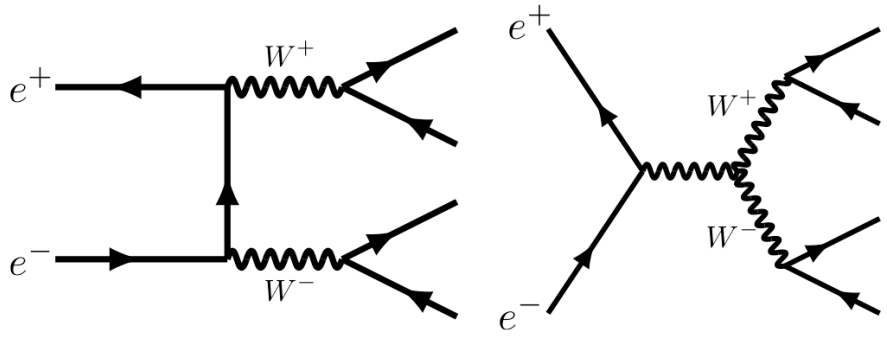

Figure 4.11: The lowest-order Feynman diagrams for semi-leptonic decay of W^+W^-

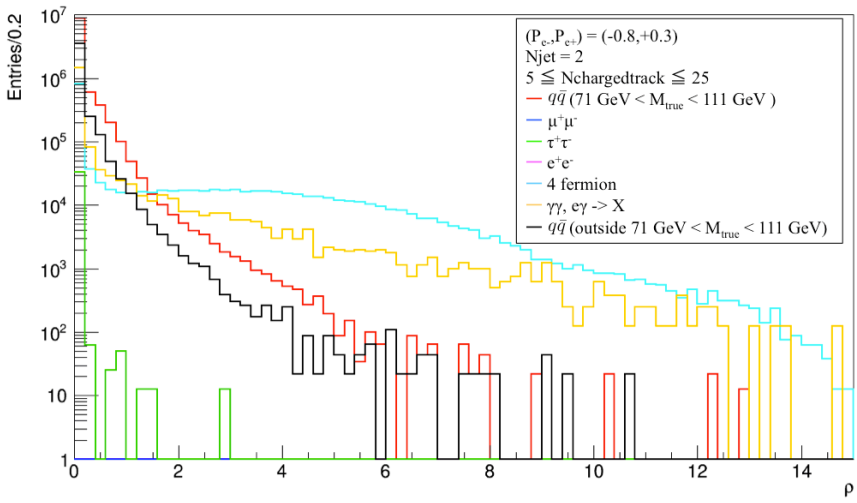

Figure 4.12: ρ distribution

Reconstructed Invariant Mass of Two Jets

The reconstructed invariant mass is defined simply as the invariant mass of the two jets

$$M^2(reco) = (P_{jet1} + P_{jet2})^2, \tag{4.15}$$

where $P_{jet1,2}$ are the 4-momentum of each jet. The $M_{2jet}(reco)$ distribution is found in Figure 4.14 and the dependence of the significance on $M_{2jet}(reco)$ in Figure 4.15

4.4 Results

Only the events satisfying the following x-window are reconstructed:

$$0.75 < x < 0.95 \tag{4.16}$$

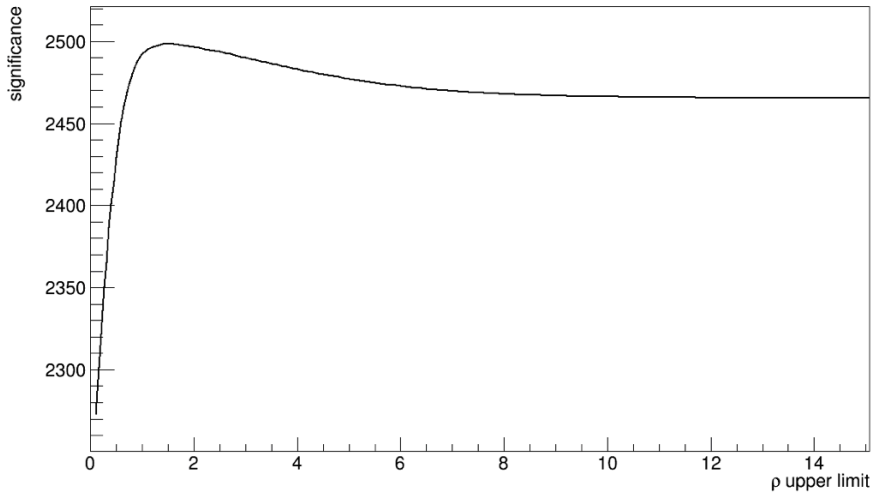

Figure 4.13: The dependence of the significance on ρ

This is determined so that the significance is maximized. The x distribution before the selection cut is shown in Figure 4.16 and one after cut in Figure 4.17. the dependence of the significance on x in Figure 4.18.

4.4.1 Derivation of the A_{LR}

Assume the MC data for background is generated correctly. The number of signal can be obtained by subtracting the number of background events based on the MC data from the measured number of all events. The x distributions of background events are found in Figure and Figure 4.20. The number of events is summarized in Table 4.4. Then, the number of

	N_L $(250\ fb^{-1})$	N_R $(250\ fb^{-1})$
All Events (measure)	10434326	6794226
All Background Events (MC)	1051278	469413

Table 4.3: Number of all events and background events

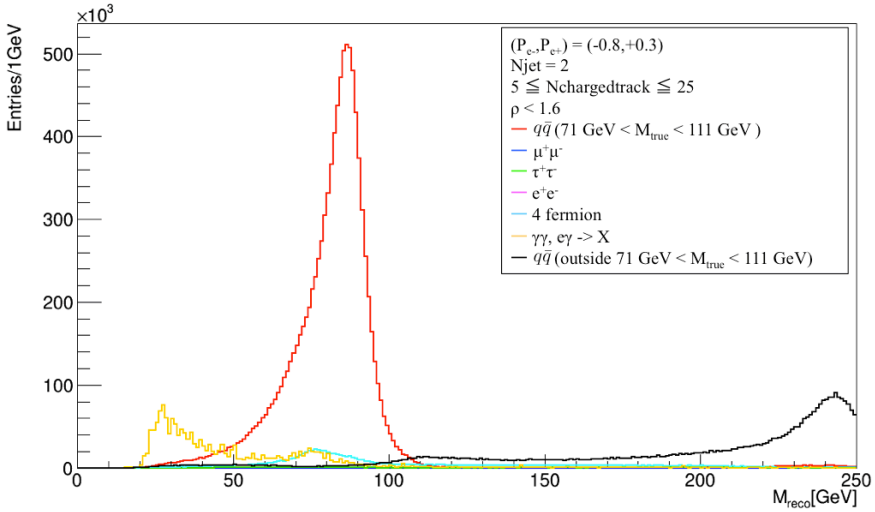

Figure 4.14: The M_{reco} distribution

signal events is derived as:

$$\begin{aligned} N_L^{signal} &= N_L^{total}(meas) - N_L^{bkg}(MC) = 9383048 \\ N_R^{signal} &= N_R^{total}(meas) - N_R^{bkg}(MC) = 6324813 \end{aligned} \tag{4.17}$$

Using these numbers, A_{LR} can be calculated as:

$$A_{LR} = \frac{N_L^{signal} - N_R^{signal}}{N_L^{signal} + N_R^{signal}} \frac{1 + \langle P_{e^-} \rangle \langle P_{e^+} \rangle}{\langle P_{e^-} \rangle + \langle P_{e^+} \rangle} = 0.21947 \tag{4.18}$$

Let us think about the statistical error of the A_{LR} value. In principle, the helicity of each bunch consisting of transferred beam is flipped randomly. Even if the random helicity is exactly 50 %, the magnitude of the luminosity can be unequal for the two helicity. Hence, Equation (1.6) is better to start with rather than Equation (1.7). Using the ratio of the magnitude of the luminosity for the two helicity, r_L, A_{LR} is expressed as

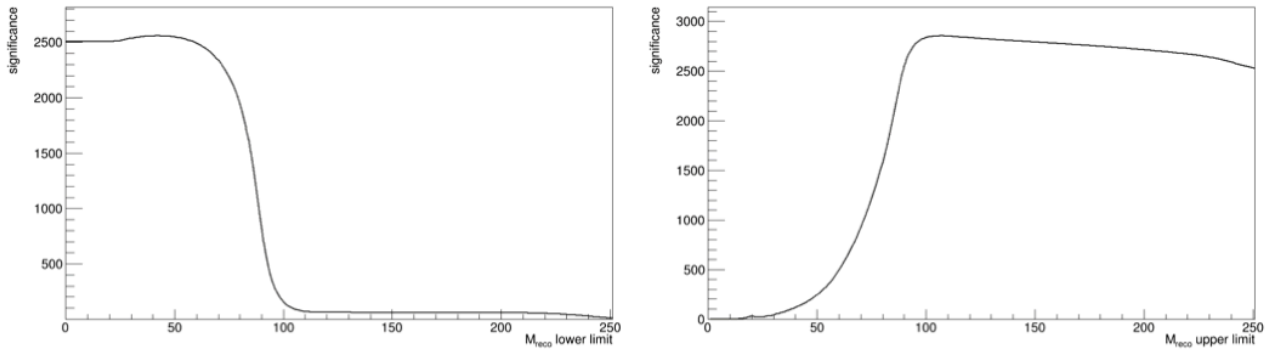

Figure 4.15: The dependence of the significance on M_{reco}

$$A_{LR} = \frac{N_L - N_R \cdot r_L}{N_L + N_R \cdot r_L} \ \frac{1 + \langle P_{e^-}\rangle\langle P_{e^+}\rangle}{\langle P_{e^-}\rangle + \langle P_{e^+}\rangle} \tag{4.19}$$

Assume that the error of polarization is so small that it is negligible. The propagation of the errors is given by

$$\begin{aligned} \Delta A_{LR} &\approx \sqrt{(\frac{\partial A_{LR}}{\partial N_L})^2(\Delta N_L)^2 + (\frac{\partial A_{LR}}{\partial N_R})^2(\Delta N_R)^2} \\ &= \frac{2N_L N_R \cdot r_L}{(N_L + N_R)^2} \ (\frac{1}{\sqrt{N_L}} + \frac{1}{\sqrt{N_R}}) \ \frac{1 + \langle P_{e^-}\rangle\langle P_{e^+}\rangle}{\langle P_{e^-}\rangle + \langle P_{e^+}\rangle} \end{aligned} \tag{4.20}$$

The statistical error of the signal events can be regarded as the square root of the number of all events. Then, the result is obtained as follow:

$$A_{LR} = 0.21947 \pm 0.00038 \ (500 fb^{-1}) \tag{4.21}$$

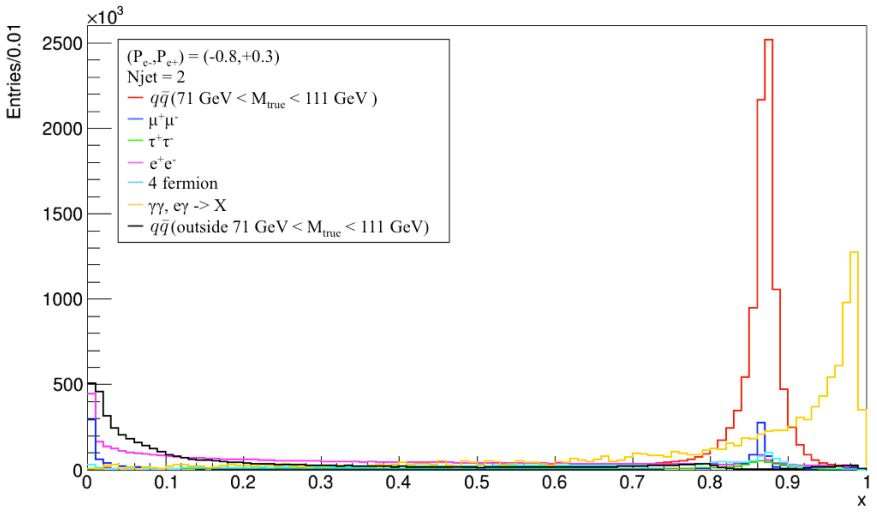

Figure 4.16: The x distribution before the selection cut with $(P_{e^-}, P_{e^+}) = (-0.8, +0.3)$

corresponding to

$$\sin^2\theta_{\mathrm{W}} = 0.22223 \pm 0.00005 \ (500 fb^{-1}) \tag{4.22}$$

DBD sample is generated with $\sin^2\theta_{\mathrm{W}}$ of 0.22225 corresponding to the A_{LR} of 0.21930. With the full-data of 250 GeV operation at the ILC, the statistical error of the A_{LR} can be reduced to be half furthermore and it corresponds to the relative statistical error of about 0.1 %.

4.4.2 Fitting

In order to remove MC modeling uncertainties for background events, the number of events is extracted from the integration of a fitting function. The x distribution for only signal events is fitted with three Gaussian functions (see Figure 4.21 and 4.22). Then, the total x distribution is fitted with the signal function, another Gaussian function and a third-order function (see Figure 4.23 and 4.24). The latter two are introduced for fitting background events. Here,

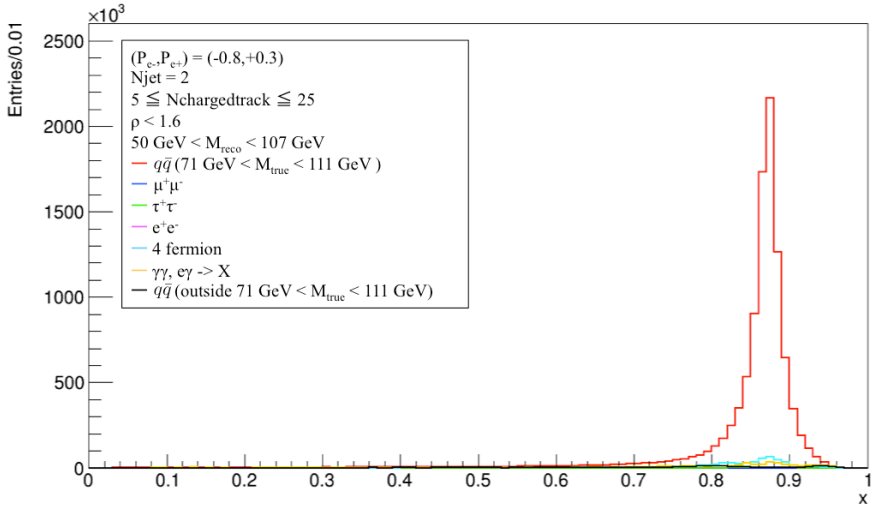

Figure 4.17: The x distribution after the selection cut with $(P_{e^-}, P_{e^+}) = (-0.8, +0.3)$

the shape of the signal function are fixed, while all parameters for the background function is floated. The result is summarized in Table 4.4.

	N_L $(250\ fb^{-1})$	N_R $(250\ fb^{-1})$	$\frac{N_L - N_R}{N_L + N_R}$	A_{LR}
All Events	10216660	6655036	0.21110	0.23797
Signal Events	9314017	6277252	0.19477	0.21956
Background Events	902643	377784	0.40991	0.46208

Table 4.4: The result of integration for each fitting function in the range of $0.75 < x < 0.95$

In the same way as before, the statistical error is obtained by

$$A_{LR} = 0.21956 \pm 0.00040\ (500 fb^{-1}) \tag{4.23}$$

corresponding to

$$\sin^2\theta_{\mathrm{W}} = 0.22222 \pm 0.00005\ (500 fb^{-1}) \tag{4.24}$$

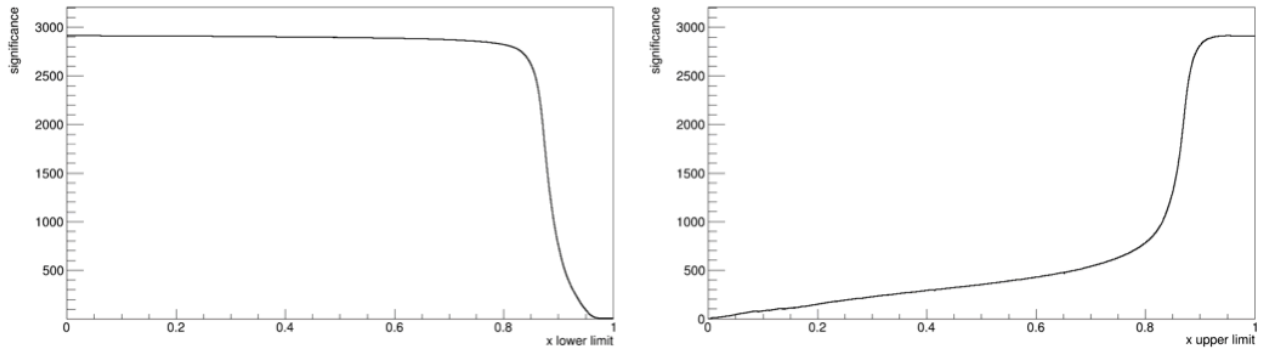

Figure 4.18: The dependence of the significance on x

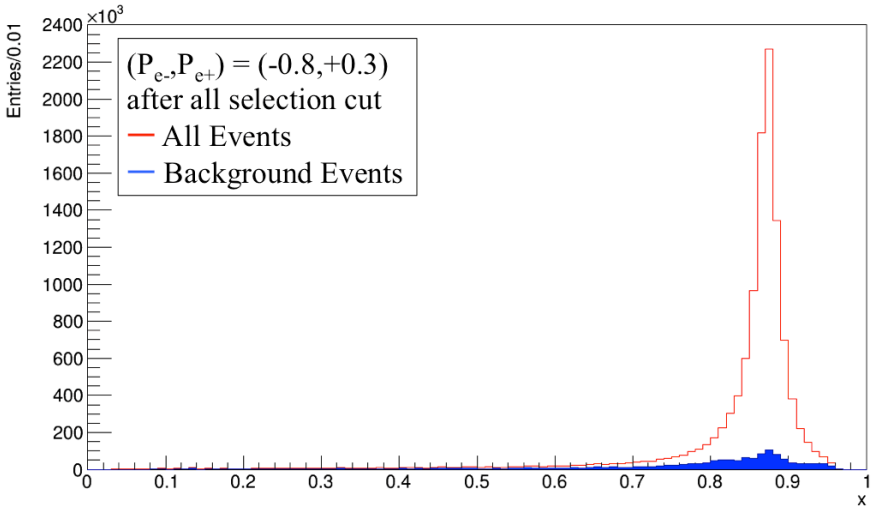

Figure 4.19: The x distribution of background events with $(P_{e^-}, P_{e^+}) = (-0.8, +0.3)$

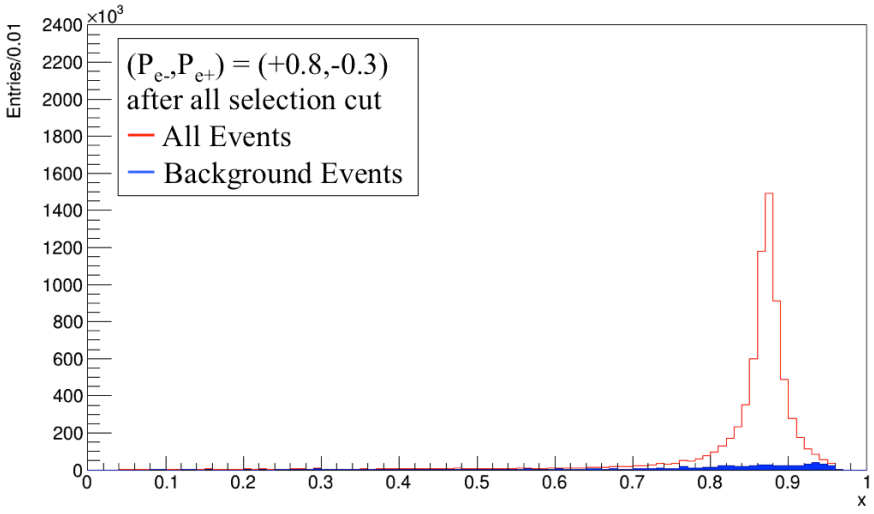

Figure 4.20: The x distribution of background events with $(P_{e^-}, P_{e^+}) = (+0.8, -0.3)$

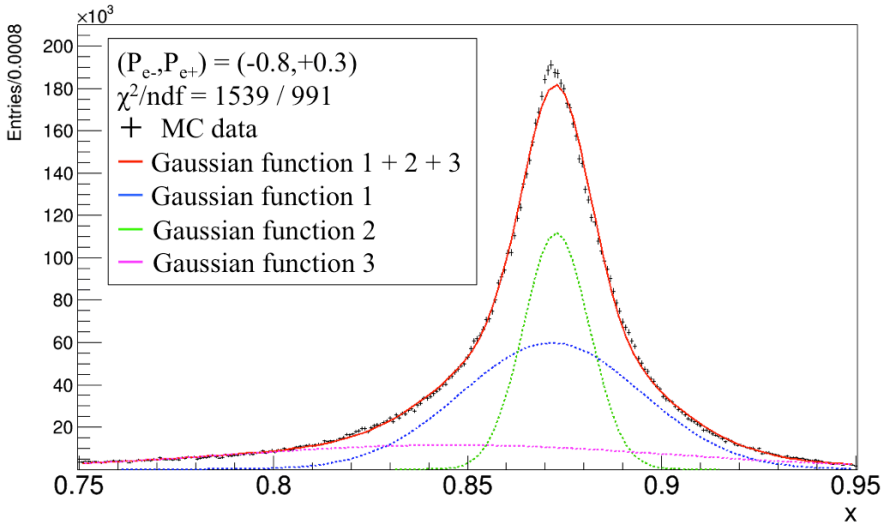

Figure 4.21: Fitting for the x distribution of signal events with $(P_{e^-}, P_{e^+}) = (-0.8, +0.3)$

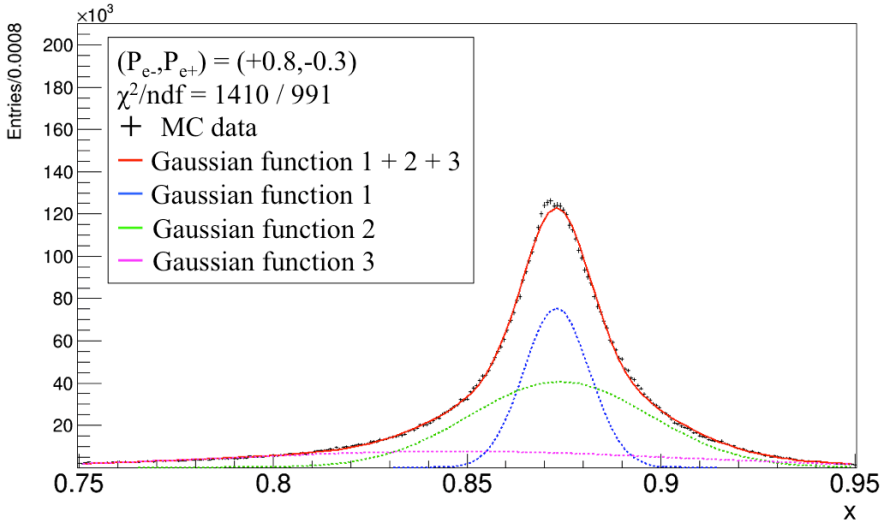

Figure 4.22: Fitting for the x distribution of signal events with $(P_{e^-}, P_{e^+}) = (+0.8, -0.3)$

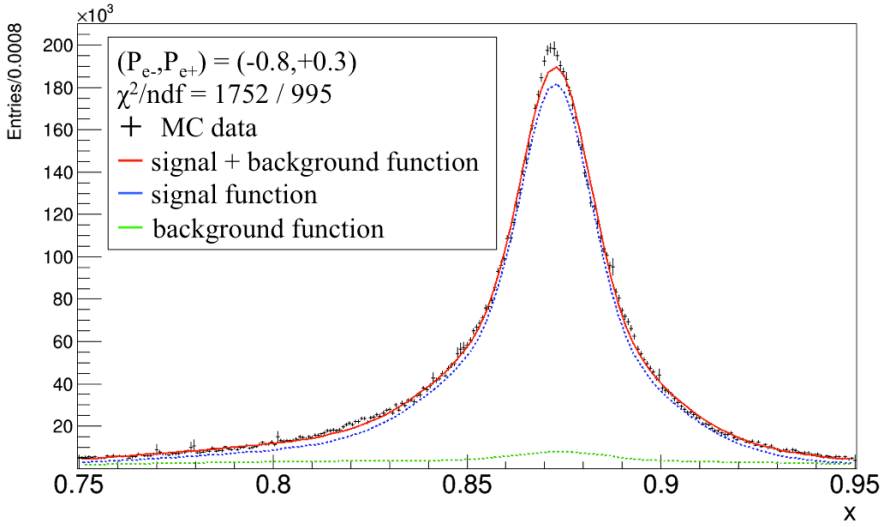

Figure 4.23: Fitting for the x distribution of total events with $(P_{e^-}, P_{e^+}) = (-0.8, +0.3)$

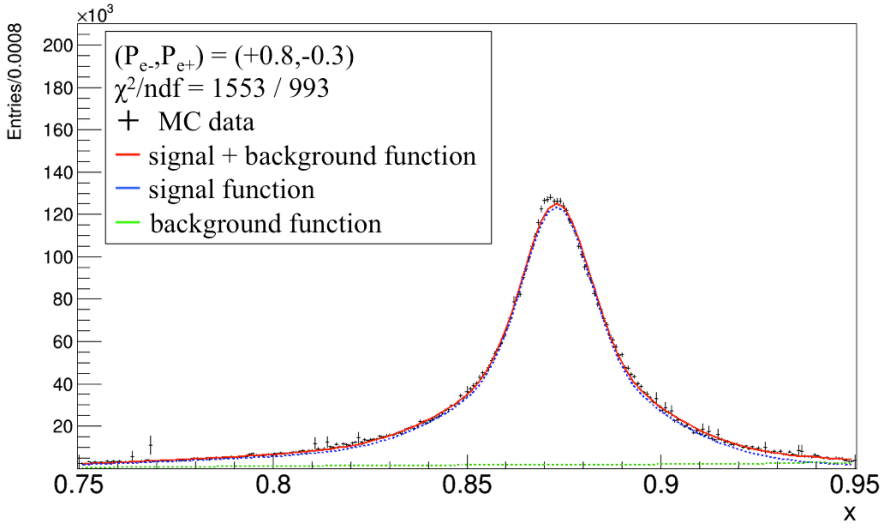

Figure 4.24: Fitting for the x distribution of total events with $(P_{e^-}, P_{e^+}) = (+0.8, -0.3)$

Chapter 5

Summary and Future Prospects

5.1 Summary

At the future linear collider ILC, the left-right asymmetry A_{LR} should be able to be measured more precisely due to improvement of beam polarization. Currently, A_{LR} has the relative error of approximately 1.5 %, which comes from the data of SLD detector at SLAC National Accelerator Laboratory.

This study is a simulation on measurement of A_{LR} using ISR at the ILC with the COM energy of 250 GeV. In this study, the signal is defined as $Z \to q\bar{q}$ event. Event reconstruction is based on the x value, which is the ratio of the ISR energy to the beam energy. As a result, with the full data at 250 GeV of 2000 fb^{-1}, the relativistic statistical error of the A_{LR} will be possible to be reduced to about 0.1%.

5.2 Future Task

There are a few things left for this study to do. While this simulation is based on the Delphes fast simulation, the full detector simulation have to be done. Then, the systematic error of this analysis should be evaluated. Regarding event generation in Whizard, as mentioned in

section 4.1.2, the photon needs to be added to the subprocess final state in Whizard in order to obtain the correct photon angular distribution.

Acknowledgement

I am very grateful to Professor Hitoshi Yamamoto for making this work possible. I also would like to thank and Professor Timothy Barklow and PhD Jan Strube and Assistant Professor Ryo Yonamine for their generous support.

Reference

[1] G. Aad et al. [ATLAS Collaboration], “Observation of a new particle in the search for the Standard Model Higgs boson with the ATLAS detector at the LHC,” Phys. Lett. B 716, 1 (2012) doi:10.1016/j.physletb.2012.08.020 [arXiv:1207.7214 [hep-ex]]

[2] K.A. Olive et al. Review of Particle Physics. Chin.Phys., C38:090001, 2014.

[3] D. Griffiths. Introduction to Elementary Particles. Physics textbook. Wiley, 2008.

[4] S. L. Glashow, “Partial Symmetries of Weak Interactions,” Nucl. Phys. 22, 579 (1961). doi:10.1016/0029-5582(61)90469-2

[5] S. Weinberg, “A Model of Leptons,” Phys. Rev. Lett. 19, 1264 (1967). doi:10.1103/PhysRevLett.19.1264

[6] A. Salam and J. C. Ward, “Weak and electromagnetic interactions,” Nuovo Cim. 11, 568 (1959). doi:10.1007/BF02726525

[7] 林　青司. 素粒子の標準模型を超えて. 丸善出版, 2015.

[8] S. Schael *et al.* [ALEPH and DELPHI and L3 and OPAL and SLD Collaborations and LEP Electroweak Working Group and SLD Electroweak Group and SLD Heavy Flavour Group], Phys. Rept. **427**, 257 (2006) doi:10.1016/j.physrep.2005.12.006 [hep-ex/0509008].

[9] T. Behnke *et al.*, “ILC TDR and DBD,” ILC-Report-2013-040. http://www.linearcollider.org/ILC/Publications/Technical-Design-Report

[10] W. Kilian, T. Ohl and J. Reuter, "WHIZARD: Simulating Multi-Particle Processes at LHC and ILC," Eur. Phys. J. C **71**, 1742 (2011) doi:10.1140/epjc/s10052-011-1742-y [arXiv:0708.4233 [hep-ph]].

[11] M. Moretti, T. Ohl and J. Reuter, "O'Mega: An Optimizing matrix element generator," hep-ph/0102195.

[12] T. Sjostrand, S. Mrenna and P. Z. Skands, JHEP **0605**, 026 (2006) doi:10.1088/1126-6708/2006/05/026 [hep-ph/0603175].

[13] M. Chrzaszcz, T. Przedzinski, Z. Was, J. Zaremba. (2016). TAUOLA of tau lepton decays– framework for hadronic currens, matrix elements and anomalous decays. Computer Physics Communications. 10.1016/j.cpc.2018.05.017.

[14] C. T. Potter, "DSiD: a Delphes Detector for ILC Physics Studies," arXiv:1602.07748 [hep-ph].

[15] The ALEPH Collaboration, "Determination of the LEP center-of-mass energy from $Z\gamma$ events" arXiv:9810047 [hep-ex].

[16] Elia, R.D. (1994). Measurement of the left-right asymmetry in Z boson production by electron-positron collisions (SLAC–429). United States